A Method for Obtaining Structural Parameters of Globular Clusters in M33 using the LBT

Raymundo Mora Jr.

This thesis is submitted in partial completion of the requirements of the BA Astronomy Major

Department Astronomy
University of Virginia

May 20, 2021

Project Advisor: Steven Majewski

Abstract

We present a method for obtaining the structural parameters of globular clusters in M33 from data obtained by the Large Binocular Telescope Observatory's LBCB and LBCR instruments. We test and develop our methods by following a structure similar to that presented on Ma (2015) and compare our results involving the same globular clusters. Our comparisons are not one-to-one and should not be treated as such. There are differences in the instrumentation involved in the observation process that will introduce inherent differences in our estimations. These differences include the fact that seeing in our instruments (i.e. the LBCB and the LBCR) is limited to a little over an arcsecond , 1.13", (see Section 7) while the HST/WFPC2 used for the the observations in Ma (2015) have a seeing of around 0.1" Sarajedini et al. (2000). Additionally we are looking through different filters which have different levels of sensitivity at different wavelengths. We find that the initial results of our developed method indicate that the strategy is sound but still needs to be altered to be able to handle a variety of sources.

1 Introduction

Because of their defining properties, globular clusters provide essential data for astronomers to probe the structure and formation processes of their host galaxies Beasley (2020). Consequentially, they serve as laboratories that are of particular interest for the study of galaxy formation and the effects of inter-galactic interactions and mergers. This information is inferred by exploring their morphological properties which serve as record keepers for their own evolution Barmby et al. (2007) and in turn that of their host galaxy.

There are over 30 galaxies in the local group with the Milky Way, M31, and M33 being among the largest. However, historically, M33 has received little attention compared to its bigger siblings (Wang & Ma (2013) & McLaughlin & van der Marel (2005)). With M33 data obtained from the LBT we have the opportunity to obtain structural parameters for the galaxy's globular clusters and from there infer more about the galactic evolution of M33. These inferences will be aided by the multitude of bands that are available to us from the LBT data given that our methods for extracting said parameters succeed. Recent studies have sparked debate on whether or not M33 is on its first bypass of M31 van der Marel et al. (2019), and the success of our methods will mean that more data can be added to aid the conversation. This will help us learn more about the interactions between M33 and M31 and their histories and in turn tell us more about the evolution of our galactic neighborhood.

Our method development will focus on the parameters derived by Ma (2015) with the F555W band from the HST/WFPC2 to formulate a way of extracting the same parameters from our LBT data. We focus on the r-SLOAN filter because of its high and stable transitivity levels at wavelengths close to the F555W band. Further work will include the rest of the LBT bands in our data starting with V-Bessel because of its similarities to the F555W band.

We work with the data for M33 clusters in Ma (2015) rather than clusters in the more expansive list in San Roman et al. (2012) because all of the clusters in Ma (2015) are halo clusters. Since we are interested in developing a method we want to test the simplest cases first. As seen in Figure 2 M33 is a crowded field so we want to start with halo clusters to begin our work with relatively isolated sources.

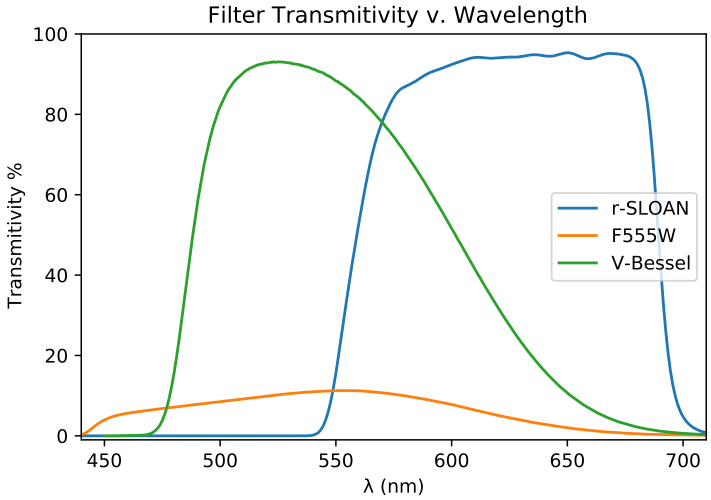

Figure 1: All four pointings are shown simultaneously here. On display are all of the 16 fully reduced frames that make our entire viewing field in the r-SLOAN band.

2 Observations

The observations for this project were submitted by Borja Anguiano of the University of Virginia to the Large Binocular Telescope Observatory (LBTO). We are concerned with the broadband observations of this submission using both the LBCB and LBCR instruments attached to the LBT. Both the LBCB and LBCR have a corrected field of view of $25' \times 23'$ at $0.225\ "/pixel$ hosting four 4608×2048 pixel detectors. The U-Bessel, B-Bessel, g-sloan, V-Bessel, and r-sloan bands of the LBCB and the i-SLOAN band of the LBCR were used to make the observations. All light frames using the LBCB were made using 60s integration times and the one band in the LBCR was made using a 180s integration time. In order to cover the entirety of M33, which has an angular size much larger than our field of view $(73' \times 45')$, four different pointings were made around the galaxy in order to maximize the amount of clusters that we can observe in every dimension. The observations were completed on two separate nights, two pointings finished observations for all six broadband filters on the night of September 18, 2017 and the other 2 pointings were completed on the night of November 17, 2017. Figure 2 shows a composite image of all four pointings in the r-SLOAN filter.

3 Data Reduction

The data were all bias-subtracted and flat-divided with high and low 3-sigmaclipping values using the IRAF distribution available through the Anaconda's Legacy Software Stack. I have found that this particular stack hosts the best installation process and distribution for IRAF currently available. The distribution uses a legacy version of IRAF based on Python 2.7 with PyRAF capabilities. This ensures that there is full compatibility with older functions of the program without the debugging required by newer distributions. Through much trial and error we have found this to be an invaluable asset as the National Optical Astronomy Observatory has ended its support of IRAF and has taken their distribution offline.

Master bias for the LBCB was generated using 29 individual bias frames for each of the four detectors. The master bias for the LBCR was generated using 22 bias frames for each of the four

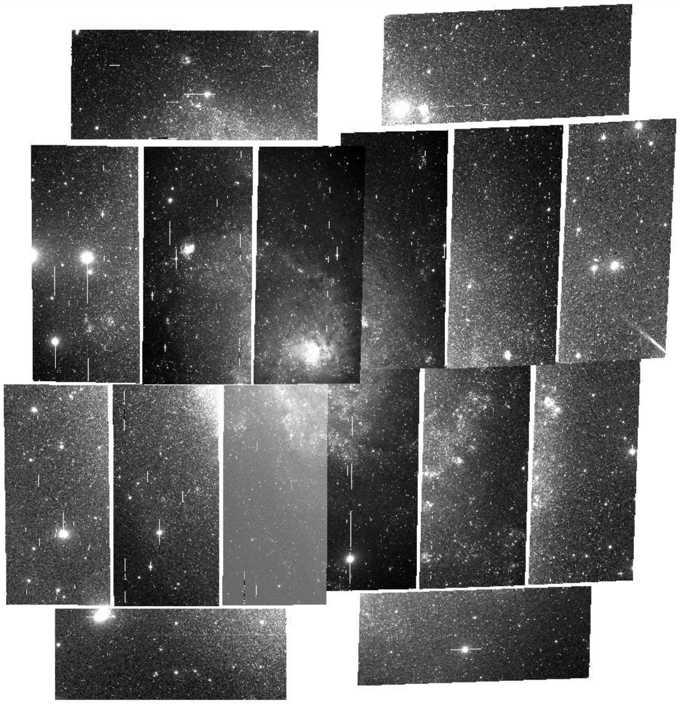

Figure 2: All four pointings are shown simultaneously here. On display are all of the 16 fully reduced frames that make our entire viewing field in the r-SLOAN band.

detectors on the instrument.

The master flats for each filter were generated using skyflats. The only dome flats available that were taken at the LBTO within a reasonable observing window to our observations only included sections of our detectors and not their entirety. Since our observations were made on two different nights separated by nearly 2 months I made two sets of master flats for every broadband filter. One set for the first two pointings using skyflats taken closer to their time of observation, and another set for the last two pointings using skyflats that were taken closer to their observation date.

Given that all of the frames taken by the LBCB and LBCR were taken at temperatures between -70.1°C and -87.4°C no dark current correction was made to any frame. At these temperatures dark current is negligible.

4 WCS

Naturally, the first step in our process involved extracting data of known sources from our observations. Locating known sources in our data with a reliable accuracy is crucial to the analysis and processing of our observations as it is the way in which we will know we are analyzing the same sources as Ma (2015) and Sarajedini et al. (2000). If the wrong sources are analyzed and mistaken for those which we are basing our methods on we will be led astray and tune our processes with improper adjustments. Additionally, proceeding without the proper coordinate system and failing to detect imperfections in our reported positions would lead to reporting of data in locations without the relevant sources.

Given the importance of locating sources with reasonable accuracy and the relevance of doing so in both the development of our methods and reporting of our findings, the first step in our analysis consisted of building a program capable of taking any list of sources with their α and δ reported in degrees and determining whether or not the source is located within the field of view of any of our four pointings found on 2. The program was made to return a list of the sources from the original which were determined to be located within our field of view along with what CCD each source is located in. Once it has defined the CCD corresponding to each source the program proceeds to read the header file for each CCD in order to convert the coordinates of each source to image pixel coordinates. Once the pixel coordinates of a source have been located the program logs the CCD containing the source, its α δ, its pixel coordinates, and returns a 100 × 100 pixel array of our data centered at the source so that the data is readily available for further analysis.

Using our program we found that there were significant problems with the WCS provided by the headers of our LBT observations. By visually inspecting the cutout data provided by our source locating program we found that the centering of our data was must be off by some factor in both dimensions given that the data that was returned often cenetered on empty areas of our CCD.

To solve our WCS problem we turned to astrometry.net (2021) to see if the trusted package could fix the problems we were seeing with the original WCS of our headers. astrometry.net (2021) uses their own index files to look for a shape similar to that which is found in your image generated by selecting four sources in your data. Once one is found in one of their index files, the program reiterates this process on more sets of four sources to narrow down the sky pointing of your data. If the algorithm succeeds it returns a FITS file with your data which includes the corrected WCS information in the header.

After processing our data through astrometry.net (2021), we returned to our source locating program and input a list of known sources and searched for them in the WCS corrected images. This procedure was successful and allowed us to move forward with the LBT data. There was suspicion that the offset present in the WCS of the LBT data was a function of pixel position within a detector and/or pixel position relative to the optic, however, we learned that the offset remained consistent throughout. We found that the WCS in the LBT data has an offset of 160”. This equates to 685pixels in the x-axis and 203pixels in the y-axis in our CCDs. This offset is visualized in Figure 3 where we show the CCD we have conventionally labeled F1C2 containing clusters C20 and M9 from Sarajedini et al. (2000).

5 Creating the Surface Brightness Profile

The creation of surface brightness profiles is essential to the generation of the structural parameters we expect to extract from the clusters presented in Sarajedini et al. (2000) and Ma (2015) so it is important that we use a trusted method for obtaining these parameters and constructing the surface brightness profiles of our sources. To achieve this we return to Bradley et al. (2020) to use the *isophote* module. Using the *isophote* module we are able to easily construct surface brightness profiles for objects that we are interested in. We do this by using the cutout data and pixel coordinates (within the cutout) for our sources of interest obtained through a program we wrote similar to our source locating script and inputting it to the relevant packages in the *isophote* module. For the additional required initial parameters we use an initial guess of a small ellipticity, small position angle, and a semi-major axis of 1.5 pixels. We find that these initial parameters are capable of finding solutions for the creation of isophotes for all point sources but fail with extended objects and require some manipulation. In addition to allowing us to obtain the measurements of our clusters we are interested in, extracting the surface brightness profile of a source is essential to obtaining the parameters that define the PSF for our observations and to perform certain checks in our methods as discussed in 6.

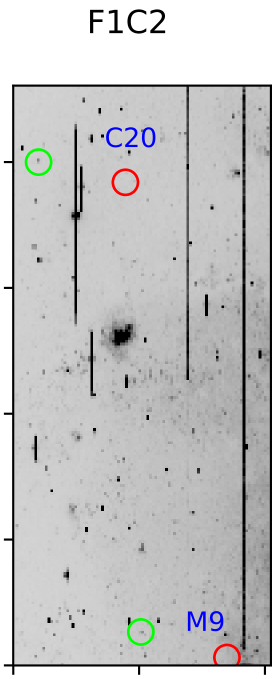

Figure 3: The red circles indicate where the WCS was pointing to in our image using the header originally produced by the LBT using the coordinates for clusters C20 and M9 Sarajedini et al. (2000). The green circles indicate where the astrometry-solved WCS point to using the coordinates for clusters C20 and M9 Sarajedini et al. (2000)

6 Background Estimation/Subtraction

As made evident by Figure 2, M33 is a crowded field and relatively few isolated sources exist within our field of view. This is good for the amount of potential sources available for analysis but potentially hurtful for the accuracy of said analysis. Because of this, before attempting to extract the surface brightness profiles of sources in our data we must have a good idea of the contamination around them and remove it in order to have what will be estimated to be the signal of our source absent of noise introduced by the background or nearby sources.

For our background estimation we used the *background* module from Bradley et al. (2020) to calculate and remove the background from our sources. We applied the function for the background estimation to our 100 × 100 pixel cutouts of relevant sources generated by our source locating program. Because of the nature of our field, we know that the background on each of our CCDs varies across them so we proceeded to use *Background2D* from the *background* module in order to obtain our 2-dimensional estimations of the background in our 100 × 100 pixel cutouts. *Background2D* achieves its background estimation by obtaining median values in different areas of the sigmaclipped data. The size of the areas are specified when the function is called, in our case we used 25 × 25 pixel areas in *Background2D* to generate 16 regions where the background is estimated. *Background2D* then generates a low resolution background image which is then interpolated to generate a final background image of the same dimensions as the input image. Utilizing smaller regions and, therefore, more regions could help the interpolation of our low-resolution background estimation, however, we must be careful that the regions remain larger than the sources present in our cutouts in order to get a proper estimation. We may develop methods to optimize the size of the background estimation regions in the future, but for now we used the aforementioned 25 × 25 pixel size regions for all of our background estimations and subtractions.

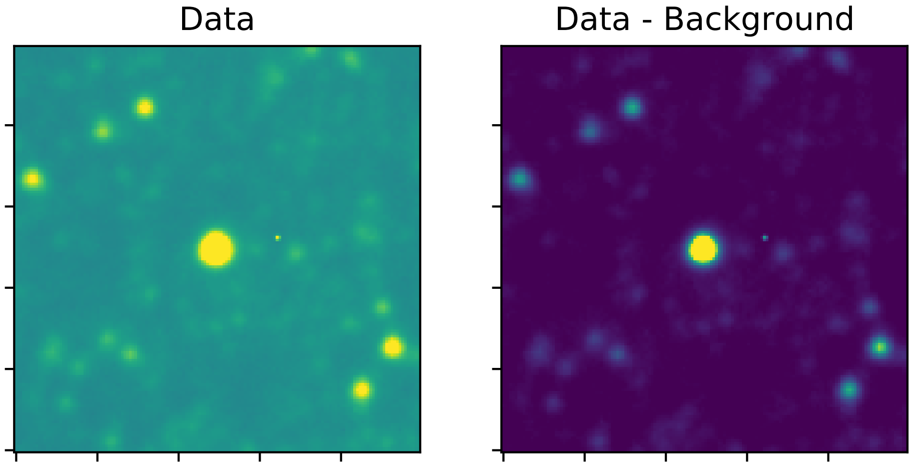

Figure 4: On the left we display what a selected star from F1C2 looks like in our fully reduced data. The data in this cutout (left) has not been background subtracted. On the right we show the background subtracted data. Both images are displayed using the same scaling as one another.

On Figure 4 we show what our background subtraction method does with one of our cutouts produced by our source locating program. The star at the center of each image on display is a randomly selected star from our list of PSF generating stars from Section 7. To get a better understanding of our background estimation, we take a look at it on Figure 5 to see how it varies across our cutout. Notice the scaling bar on the right had side of the image. It seems that our background values are mostly uniform across the cutout and range at a maximum of 40 ADU.

To determine whether we performed a background subtraction that we can trust or if we need to revisit our methods and possibly alter our initial parameters built the surface brightness profile for the star plotted in Figure 4 using the "RAW" and background subtracted data. The surface brightness profiles were obtained using the methods described in Section 5 and displayed on Figure 6.

We are curious to whether or not we obtained a trusted estimate for the background so we used figures like Figure 6 to visually inspect the background estimation for multiple sources in our data. It was concluded that we could proceed with our methodology given that they all returned values like those seen in Figure 6. That is, our visual inspection of the background estimations using surface brightness profiles showed that our background subtracted data would always asymptote to a zero level brightness at expected radii. Using the fact that the profiles level off to 0 ADU at larger radii qualifies as a good way to check the background subtraction because the principle reason for wanting

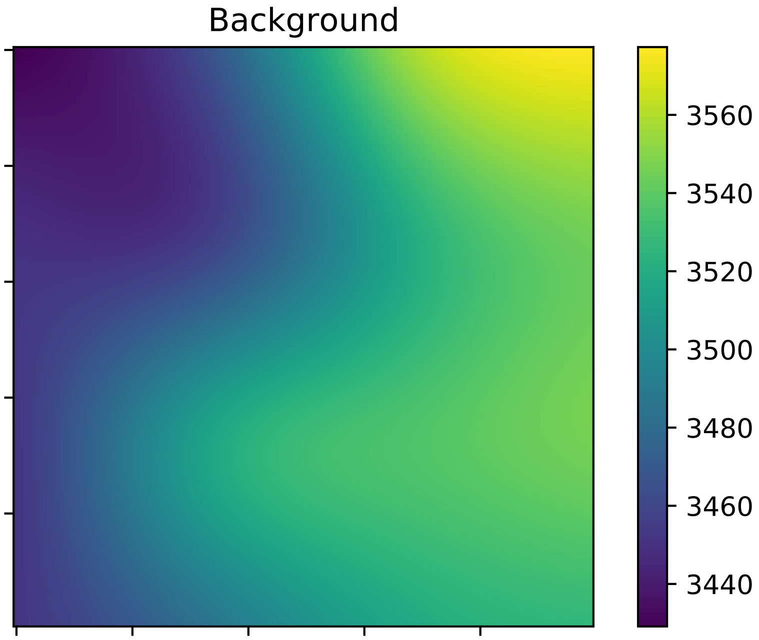

Figure 5: Background estimated from the cutout on the left side of Figure 4 using the methods described in Section 6.

a source absent of background noise is to obtain data that is as close as solely representative of the source in question. When looking at an isolated source (i.e. a source with no light from any other object in its field) and plotting its surface brightness profile we expect it to approach zero as the radii increases and the closer that source is to a point source (e.g. a star) the faster it should approach it. Having constructed a method for performing the background subtraction that we are satisfied with we proceeded to apply it to all of our sources of interest before extracting their surface brightness profiles and continuing with the analysis.

7 PSF Fittings & Deconvolution

Much like the way background noise is present in all of our data, so is another form of noise that is this time introduced by instrument rather than the sky itself, seeing. For every object that our instrument+optics observe there is a from in which it inherently ”smears” the light in the actual data. The best estimation for this ”smearing” is obtained by paying close attention to how spread (”smeared”) point sources are.

To begin the creation of the point spread functions for our observations we submitted a query to Gaia DR3 in an attempt to obtain a list of stars within our field of view which could be sorted by CCD location through our source locating program. We looked for sources with $15.5 < V < 18.5$ to ensure we remained within the dynamic range of our data in the r-SLOAN band. Further, to try to make sure we had stars in our list, looked for sources with a relatively high proper motion. This yielded a small list of 70 sources. Once we ran these sources through our source locating program we found that < 5 sources were returned. We found that the program based on Astropy Collaboration

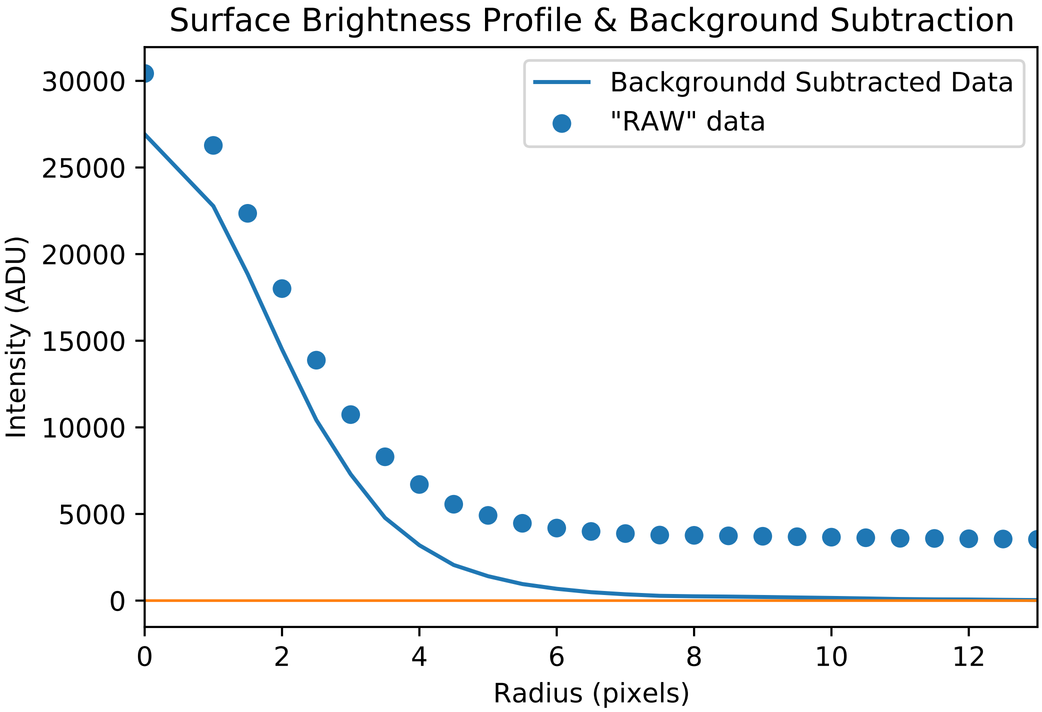

Figure 6: The surface brightness profile for the star displayed on Figure 4. The dot markers represent the surface brightness obtained from the reduced non-background subtracted data. The solid blue line indicates the surface brightness obtained from the reduced background subtracted data. The orange line is a visual aid marking zero-level brightness.

et al. (2018) failed for objects that were further than 8000 pixels from the center of any given CCD.

To work around this we used DS9 to manually select stars for the creation of our PSF for the CCD containing clusters C20 and M9 Sarajedini et al. (2000). The surface brightness profiles of these stars can be seen on Figure 7.

Using the 16 stars found manually we averaged their intensities at each radii to obtain the average surface brightness profile for stars in the CCD. Using this averaged profile we fit Equation 1 from Wang & Ma (2013) to obtain the parameters that define the dimensionless PSF of our CCD. For F1C2 the values were: $r_0 = 5.95$, $\alpha = 2.12$, and $\beta = 12.93$. The result of this fitting can be seen on Figure 8. The PSF for the CCD revealed that we have a seeing of 1.13”.

$$I_{PSF}/I_0 \;=\; [1 + (R/r_0)^{\alpha}]^{-\beta/\alpha} \tag{1}$$

Knowing that any source is affected by the ”smearing” caused by our optics+instrumentation we must take it into account in any non-point source of interest that we want to inspect (e.g. globular clusters). The way it is presented and accounted for in Ma (2015) and other studies is by convolving the PSF function like the one we found earlier with the function we wish to fit, in our case the most general form of the King profile King (1966). If we convolve the two functions we will essentially be able to add at each point of our King fitting the effects introduced by the PSF of the exposure and account for what it does to our surface brightness profiles before attempting to extract the characteristic parameters of a source. However, doing this proved rather difficult to achieve in the scope of this paper. Since we weren’t able convolve the two functions before analyzing the data, we

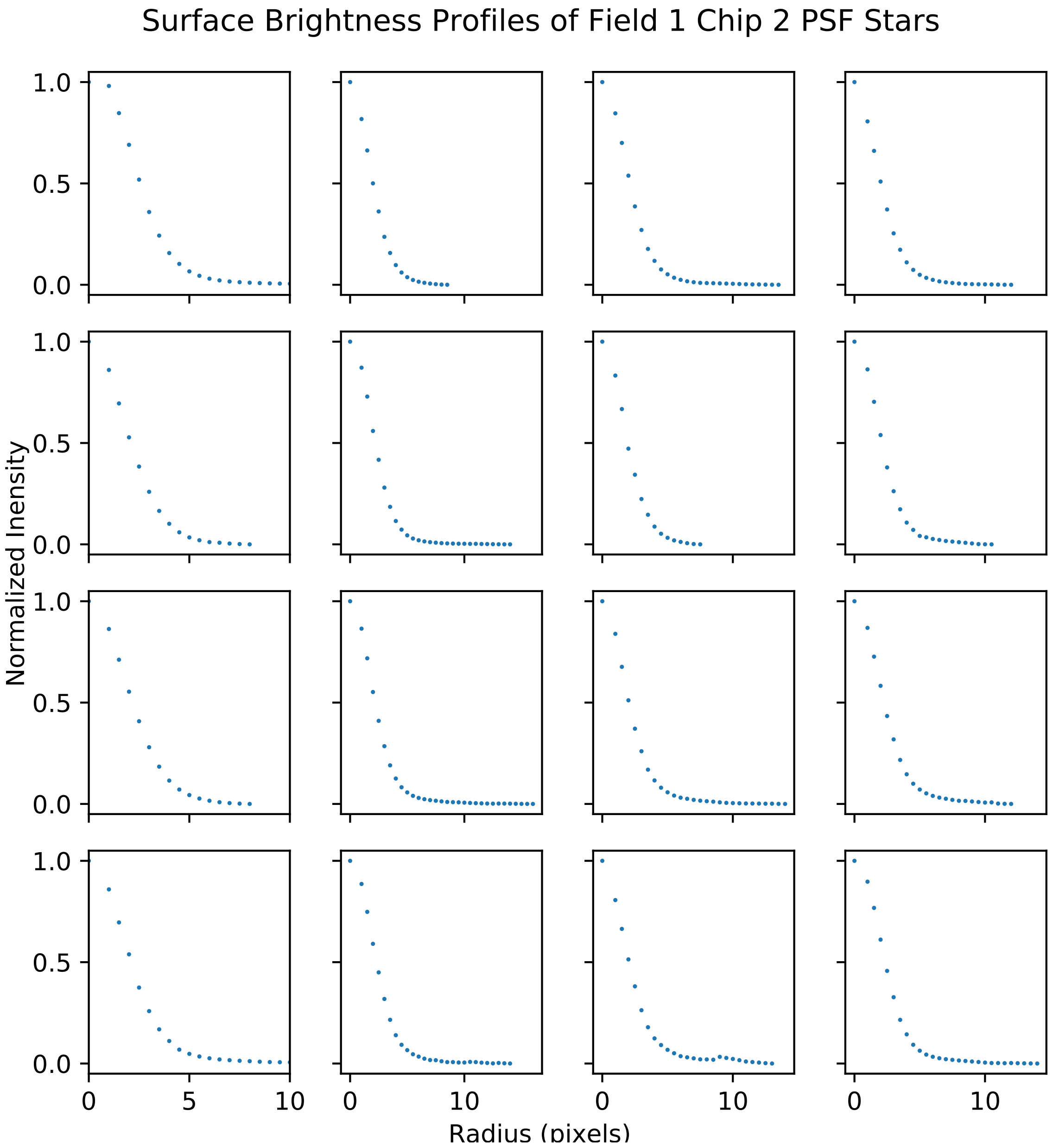

Figure 7: The surface brightness profiles of the 16 stars used to create the PSF for the CCD containing M9 and C20 as seen on Figure 3. The PSF created using the 16 stars above can be found on Figure 8.

decided to deconvolve the PSF from the data before fitting our King profiles. The author would like to thank L. Beale for his contributions to the program and methods involved in the deconvolution. The process relies on the Richardson-Lucy algorithm for deconvolution. Once we are able to deconvolve the PSF from our data (i.e. remove the effects of seeing from our data) we end with data that has been background subtracted and absent of ”smearing” caused by the nature of the instrumentation. The residual data is our best estimation of the representation of the source of interest and is now ready to be fitted to our empirical model, the King profile.

Figures 9 and 10 show the disparity in our estimations for the core and tidal radii when the PSF is not taken into account. Both axes on these plots are in $\log_{10}$ space so the actual differences in the

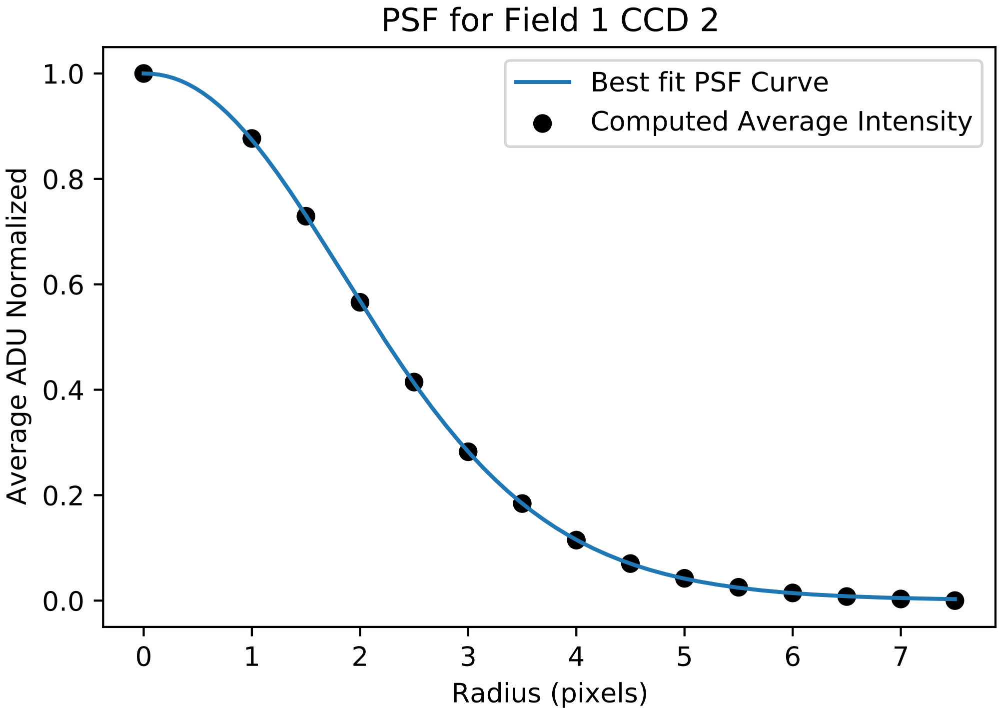

Figure 8: The PSF created

estimations are much larger than they appear. In the next section we will check if all of our methods that have been described up to this point have led to the development of a sound method of extracting structural parameters of globular clusters in M33 from LBT data.

8 Results

After subtracting the background from a fully reduced 100 × 100 pixel cut out centered at cluster C20 Sarajedini et al. (2000), subtracting the local background and deconvolving the PSF of its host CCD we fit the most general form of the King profile King (1966) to extract its core and tidal radii. In Figure 11 we see the difference in the the core radii estimations for C20 between the deconvolved data and the data containing the PSF of the exposure. The deconvolved estimation shows a significant improvement and shows a value with error bars that are just outside of the one-to-one line. Using the same methods and initial parameters yielded a value for the tidal radius of C20 that was smaller than the core radius. Additionally, with these initial conditions, inconsistent values were reported for M9. Through brute trial and error, some initial parameters yielded parameters that were closer to what we expected for the two clusters in F1C2.

9 Conclusion & Discussion

Based on the success of the first pass on our first cluster, C20, it appears that we are on the right path to developing a method for extracting morphological parameters of M33 in our LBT data. However, multiple passes on C20 and later M9 revealed that the fittings are heavily reliant on the

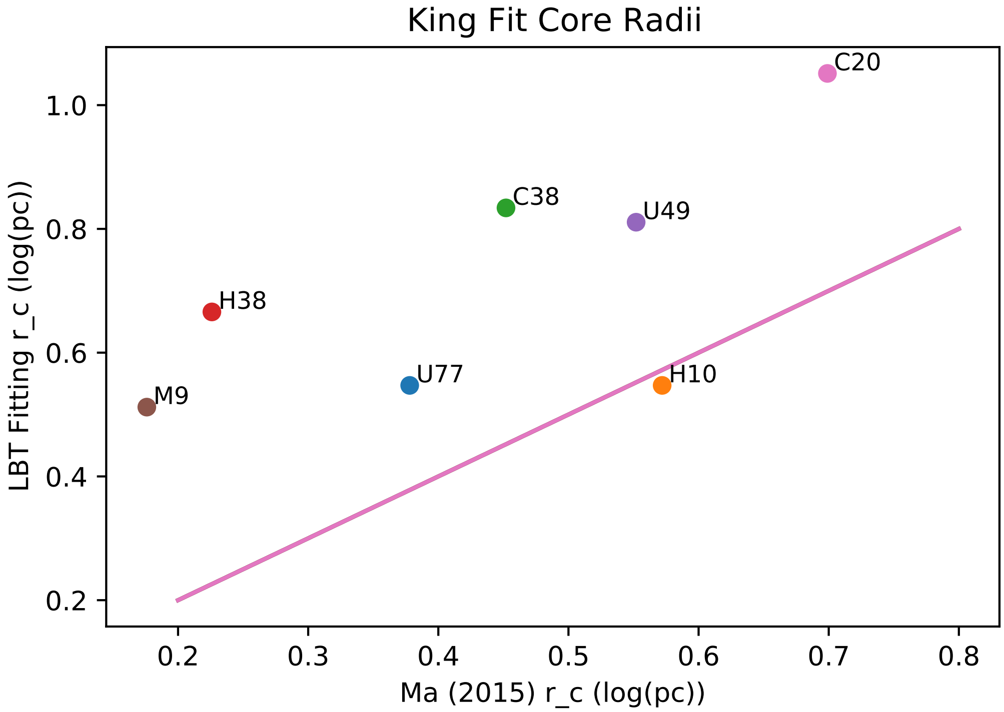

Figure 9: In this figure we present the core radii we were able to extract from the clusters in Ma (2015) plotted against the core radii as reported by Ma (2015). Note that both axes are plotted in $\log_{10}$ space. The errors are too small to appear in this space. The solid line is the one-to-one line and where we expect our values to center around.

initial parameters of our *isophote* fitting function. The initial conditions that produced the results from Figure 11 returned a tidal radius that is invalid (r_t cannot be less than r_c). A different set of initial conditions returned tidal radius for C20 that was closer to the expected value but skewed the estimation for the core radius. Inspection has been performed to try to reveal whether this means that we must obtain our core and tidal radii separately or if this is unique to some extended objects.

To expand our analysis and increase our certainty about the validation of our methods the rest of the clusters from Ma (2015) and Sarajedini et al. (2000) will be analyzed next in the r-SLOAN filter of our observations. Once this is completed we plan on running the same analysis using the V-Bessel band next. As seen in Figure 1 The V-Bessel filter is the filter that extends over virtually the same wavelength sensitivities as F555W from the HST/WFPC2 HST (2021) albeit with a more variable transitivity than r-SLOAN. From here the method will be further developed using all six broadband filters available in our LBT data with the same sample of clusters that have been discussed. We prefer these clusters for the development of our methods because they are halo clusters and therefore further from the crowded fields closer to the M33 nucleus. Using these clusters as our comparison sample is preferable to using larger catalogs like San Roman et al. (2012) for this very reason.

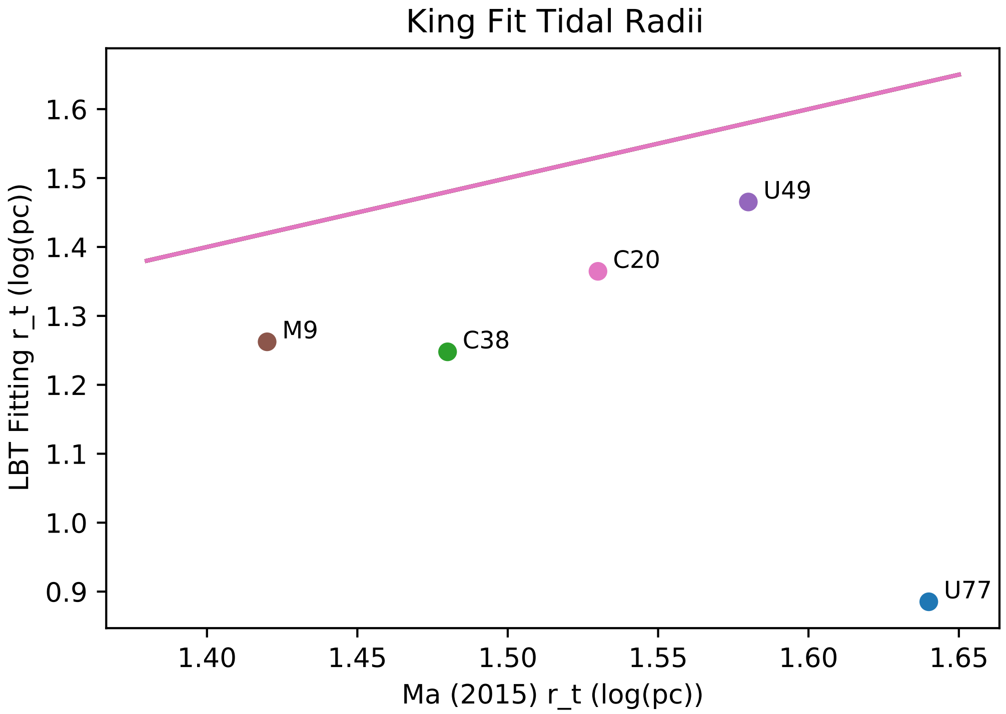

Figure 10: In this figure we present the tidal radii we were able to extract from the clusters in Ma (2015) plotted against the core tidal as reported by Ma (2015). Note that both axes are plotted in $\log_{10}$ space. The errors are too small to appear in this space.The solid line is the one-to-one line and where we expect our values to center around.

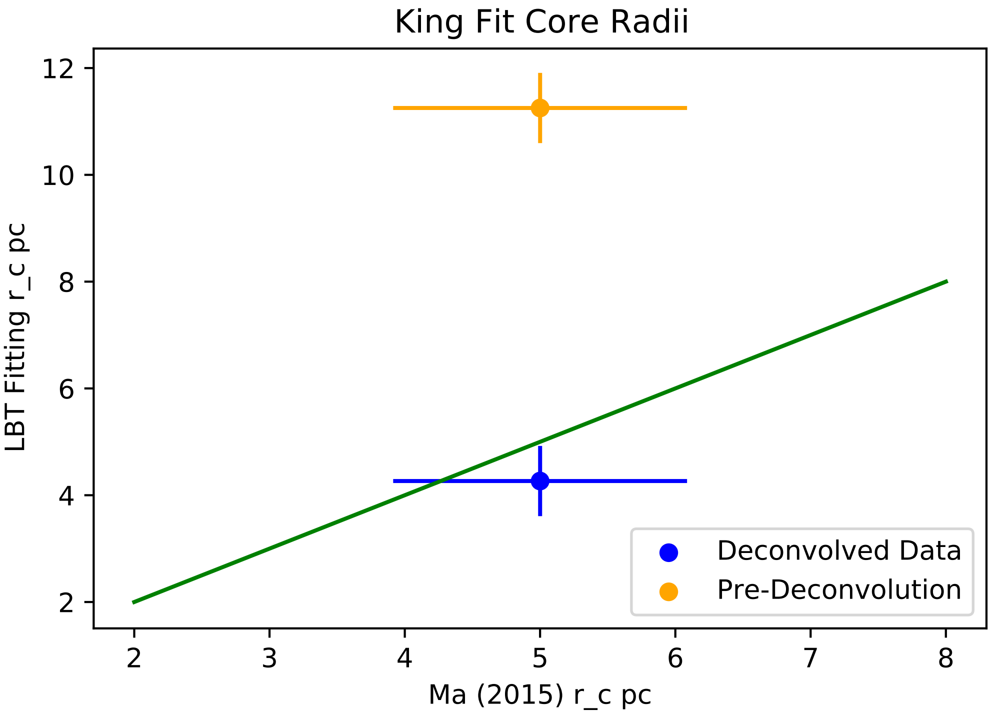

Figure 11: In orange we have our estimated core radius for cluster C20 Sarajedini et al. (2000) before the PSF was deconvolved from the data plotted against the core radii reported in Ma (2015), the same values as seen for C20 in Figure 9. The blue marker indicates our estimated core radius after the PSF was deconvolved from the data plotted against the core radii reported in Ma (2015). In blue we have the one-to-one line where we expect our values to center around.

References

astrometry.net. 2021. http://astrometry.net/

Astropy Collaboration, Price-Whelan, A. M., Sipőcz, B. M., et al. 2018, , 156, 123, doi: 10.3847/1538-3881/aabc4f

Barmby, P., McLaughlin, D. E., Harris, W. E., Harris, G. L. H., & Forbes, D. A. 2007, The Astronomical Journal, 133, 2764, doi: 10.1086/516777

Beasley, M. A. 2020, Reviews in Frontiers of Modern Astrophysics, 245–277, doi: 10.1007/978-3-030-38509-5_9

Bradley, L., Sipőcz, B., Robitaille, T., et al. 2020, astropy/photutils: 1.0.0, 1.0.0, Zenodo, doi: 10.5281/zenodo.4044744

HST. 2021, In-Flight Instruments¶. https://stsynphot.readthedocs.io/en/latest/stsynphot/appendixb_inflight.html#wfc3

King, I. R. 1966, , 71, 64, doi: 10.1086/109857

Ma, J. 2015, The Astronomical Journal, 149, 157, doi: 10.1088/0004-6256/149/5/157

McLaughlin, D. E., & van der Marel, R. P. 2005, The Astrophysical Journal Supplement Series, 161, 304, doi: 10.1086/497429

San Roman, I., Sarajedini, A., Holtzman, J. A., & Garnett, D. R. 2012, Monthly Notices of the Royal Astronomical Society, 426, 2427, doi: https://doi.org/10.1111/j.1365-2966.2012.21400.x

Sarajedini, A., Geisler, D., Schommer, R., & Harding, P. 2000, The Astronomical Journal, 120, 2437, doi: 10.1086/316807

van der Marel, R. P., Fardal, M. A., Sohn, S. T., et al. 2019, The Astrophysical Journal, 872, 24, doi: 10.3847/1538-4357/ab001b

Wang, S., & Ma, J. 2013, The Astronomical Journal, 146, 20, doi: 10.1088/0004-6256/146/2/20